

Cu-doping SnO₂-NiO p-n Heterostructure for Significant Raman Enhancement with EF > 10¹⁰: Toward Ultrasensitive VOCs Sensing

Yang Tian (✉ ytian@chem.ecnu.edu.cn)

East China Normal University

Yan Zhou

East China Normal University

Qingyi Gu

East China Normal University

Tianzhu Qiu

Jiangsu Province Hospital

Xiao He

East China Normal University <https://orcid.org/0000-0002-4199-8175>

Jinquan Chen

East China Normal University <https://orcid.org/0000-0003-0652-1379>

Ruijuan Qi

East China Normal University

Rong Huang

East China Normal University

Tingting Zheng

East China Normal University

Article

Keywords: Surface Enhanced Raman Scattering, Chemical Mechanism, Enhancement Factor, Charge-separation Efficacy, Porous Sponge Structure, Biomarker Screening

Posted Date: February 17th, 2021

DOI: <https://doi.org/10.21203/rs.3.rs-199935/v1>

License:   This work is licensed under a Creative Commons Attribution 4.0 International License.

[Read Full License](#)

Cu-doping SnO₂-NiO p-n Heterostructure for Significant Raman Enhancement with EF > 10¹⁰: Toward Ultrasensitive VOCs Sensing

Yan Zhou¹, Qingyi Gu², Tianzhu Qiu³, Xiao He^{2,5}, Jinquan Chen¹, Ruijuan Qi⁴, Rong Huang⁴, Tingting Zheng^{2*} and Yang Tian^{1,2*}.

¹State Key Laboratory of Precision Spectroscopy, East China Normal University, Dongchuan Road 500, Shanghai 200241, China.

²Shanghai Key Laboratory of Green Chemistry and Chemical Processes, Department of Chemistry, School of Chemistry and Molecular Engineering, East China Normal University, Dongchuan Road 500, Shanghai 200241, China.

³Oncology department, Jiangsu Province Hospital, Guangzhou Road 300, Nanjing 210000, China.

⁴Key laboratory of Polar Materials and Devices (MOE), Department of Optoelectronics, East China Normal University, Dongchuan Road 500, Shanghai 200241, China.

⁵Shanghai Engineering Research Center of Molecular Therapeutics and New Drug Development, School of Chemistry and Molecular Engineering, East China Normal University, Shanghai, 200062, China.

E-mail: tzheng@chem.ecnu.edu.cn; ytian@chem.ecnu.edu.cn.

Surface enhanced Raman scattering (SERS) based on chemical mechanism (CM) has attracted tremendous attention for its great selectivity and stability. However, extremely low enhancement factor (EF) limits its practical applications for trace detection. Here, a novel sponge-like Cu-doping SnO₂-NiO p-n semiconductor heterostructure (SnO₂-NiOx/Cu), was first designed and created as a CM-based SERS substrate with a significant EF of 1.66×10^{10} . This remarkable EF was mainly attributed to the enhanced charge-separation efficacy of p-n heterojunction and charge transfer resonance resulted from Cu doping. Moreover, the porous sponge structure enriched the probe molecules, resulting in further SERS signals magnification. By immobilizing copper phthalocyanine as an inner-reference element, SnO₂-NiOx/Cu was developed as a SERS nose for selective recognition of multiple lung cancer related-volatile organic compounds (VOCs) down to ~ppb level. The information of VOCs was recorded in a barcode, demonstrating practical potential of a desktop SERS device for biomarker screening.

Surface-enhanced Raman scattering (SERS) has been widely utilized as a promising analytical technique for trace detection¹. Each breakthrough in the SERS field is inseparable from the development of the enhancement substrates. Conventional SERS substrates based on electromagnetic mechanism (EM)², such as Au and Ag, exhibit ultrahigh Raman enhancement with enhancement factor (EF) up to 10^{12} . However, the EM-based SERS effect has no selectivity for Raman reporters, resulting in complicated signal outputs³. Another SERS mechanism is chemical mechanism (CM), which relies on the charge transfer (CT) processes between adsorbed molecules and SERS substrate⁴. Today, due to the high molecule selectivity and signal reproducibility, the development of CM-based SERS substrates, such as metal oxides⁵, graphene⁶, and other semiconductors⁷ has attracted more attention. Unfortunately, the CM-based SERS effect shows relatively low EFs (10^3 - 10^5) since the CT process is a short-range one⁸. The poor charge separation in CM-based SERS substrates is a major limitation, hindering further enhancement of their SERS performance⁹.

Here, a sponge like Cu-doping NiO (NiOx/Cu)-SnO₂ p-n semiconductor heterostructure (SnO₂-NiOx/Cu) was designed and created as a CM-based SERS substrate with extremely high Raman enhancement (EF= 1.66×10^{10}). The SnO₂-NiOx/Cu heterostructure was confirmed at the atomic resolution scale by aberration-corrected scanning transmission electron microscopy (ACSTEM). This notable EF value was mainly attributed to a CT process with high efficiency generated by the integration of p-n heterojunction and Cu doping, and enrichment of probe molecules by the porous nanosponge structure of SnO₂-NiOx/Cu, as illustrated in Fig. 1. The selective Cu doping on NiO narrowed the band gap through Fermi-level alignment, leading to the conversion from type-I SnO₂-NiO heterojunction into type-II SnO₂-NiOx/Cu heterojunction¹⁰. This structure ensured the delivery of photo-generated electrons from NiOx/Cu to SnO₂ and holes from SnO₂ to NiOx/Cu, further facilitating the separation of photogenerated electron-hole pairs¹¹. Furthermore, the narrower bandgap of NiOx/Cu also realized CT resonance to promote the CT process. The enhanced charge-separation efficacy of type-II p-n heterojunction and CT resonance resulted from Cu doping led to incredible SERS performance improvement on SnO₂-NiOx/Cu with an EF 10^7 times higher than that on SnO₂-NiO. This CT process was verified by density functional theory (DFT) calculation and time-resolved diffuse reflectance (TDR) spectroscopic measurements¹². The present high-EF SnO₂-NiOx/Cu substrate was then developed as a SERS nose (SnO₂-NiOx/Cu-CuPc) through immobilization of copper phthalocyanine (CuPc) as an inner-reference element for volatile organic compounds (VOCs) sensing. Exploiting the target molecular vibrational fingerprint and the well matching degree of energy level between target molecules and SnO₂-NiOx/Cu, our SERS nose showed excellent selectivity to 'sniff out' and simultaneously quantify multiple toxic VOCs in the exhaled breath (EB) of early stage lung cancer patients at ~ppb level, which was 10 times lower than those obtained by gas chromatography-mass spectrometry (GC-MS)¹³ and fluorescence spectroscopy¹⁴, 100 times lower than those obtained by electrochemical methods¹⁵. A visual diagnostic report on the concentration of toxic VOCs was obtained by SERS mapping and their corresponding barcodes. This new avenue shows great potential for developing accurate, fast, easy and cost-effective diagnosis instruments for screening of early-stage lung cancer.

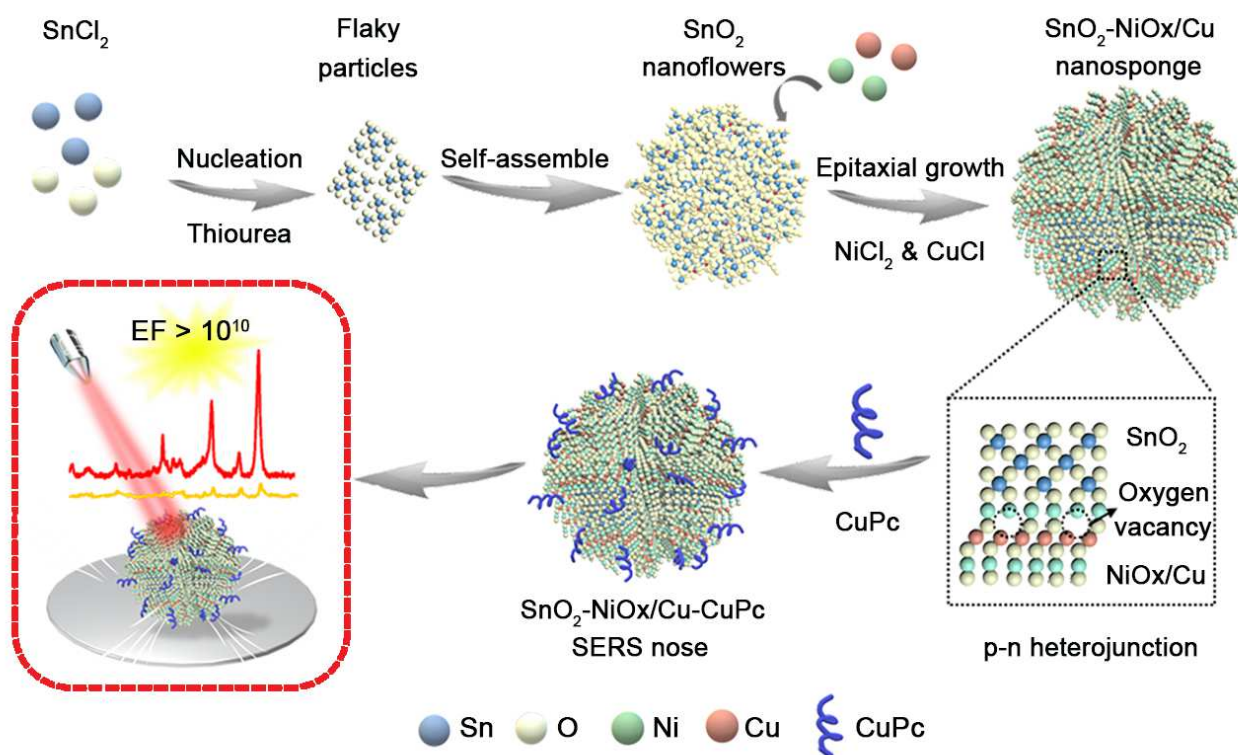


Fig. 1 Design and synthesis of a sponge-like Cu-doping SnO₂-NiO p-n semiconductor heterostructure (SnO₂-NiOx/Cu) for Raman enhancement. SnO₂-NiOx/Cu nanosponge was obtained using a hydrothermal method combined with a subsequent calcination. It was designed and created as a CM-based SERS substrate with extremely high Raman enhancement (EF=1.66 × 10¹⁰) using CuPc as a prototype probe molecule under 785 nm laser excitation.

Characterization and SERS Performance of SnO₂-NiOx/Cu

The sponge like SnO₂-NiOx/Cu p-n heterostructure was first designed and synthesized through a hydrothermal method combined with a subsequent calcination. As shown in scanning electron microscopic (SEM) image (Fig. 2a), the as-prepared porous SnO₂-NiOx/Cu nanosponges were highly uniform with diameter of 1.5 ± 0.1 μm (n=15) (Supplementary Fig. 1a). The SERS activity of SnO₂-NiOx/Cu was evaluated using CuPc as a prototype probe molecule under 785 nm laser excitation. Remarkably, the prominent signal peak at 1530 cm⁻¹ corresponding to the in-plane ring symmetric nonmetal bound N-C stretch of CuPc (10⁻⁵ M)¹⁶ was detected on SnO₂-NiOx/Cu, while on SnO₂-NiO, SnO₂ (for details, see Supplementary Fig. 2 and 3) and bare Si substrates, the signals were almost undetectable (EF < 2.15 × 10³) (Fig. 2b and 2c). The EF of SnO₂-NiOx/Cu for CuPc was calculated to be as high as 1.66 × 10¹⁰ (for calculation details, see Supplementary Methods), which was the highest EF of CM-based substrates reported to date (Supplementary Table 1).

This remarkable EF was deduced to be mainly ascribed to p-n junction of SnO₂-NiOx/Cu formed by p-type NiOx/Cu and n-type SnO₂. In the Mott-Schottky plot, the p-n junction characteristic was observed with an inverted “V-shape” (Supplementary Fig. 5a)¹⁷. The precise p-n heterostructure of SnO₂-NiOx/Cu was further explored by ACSTEM high angle annular dark field imaging (HAADF) (Fig. 2e-g). The lattice fringes corresponding to (110) plane of tetragonal phase SnO₂¹⁸ and (111) plane of NiOx/Cu¹⁹ were clearly

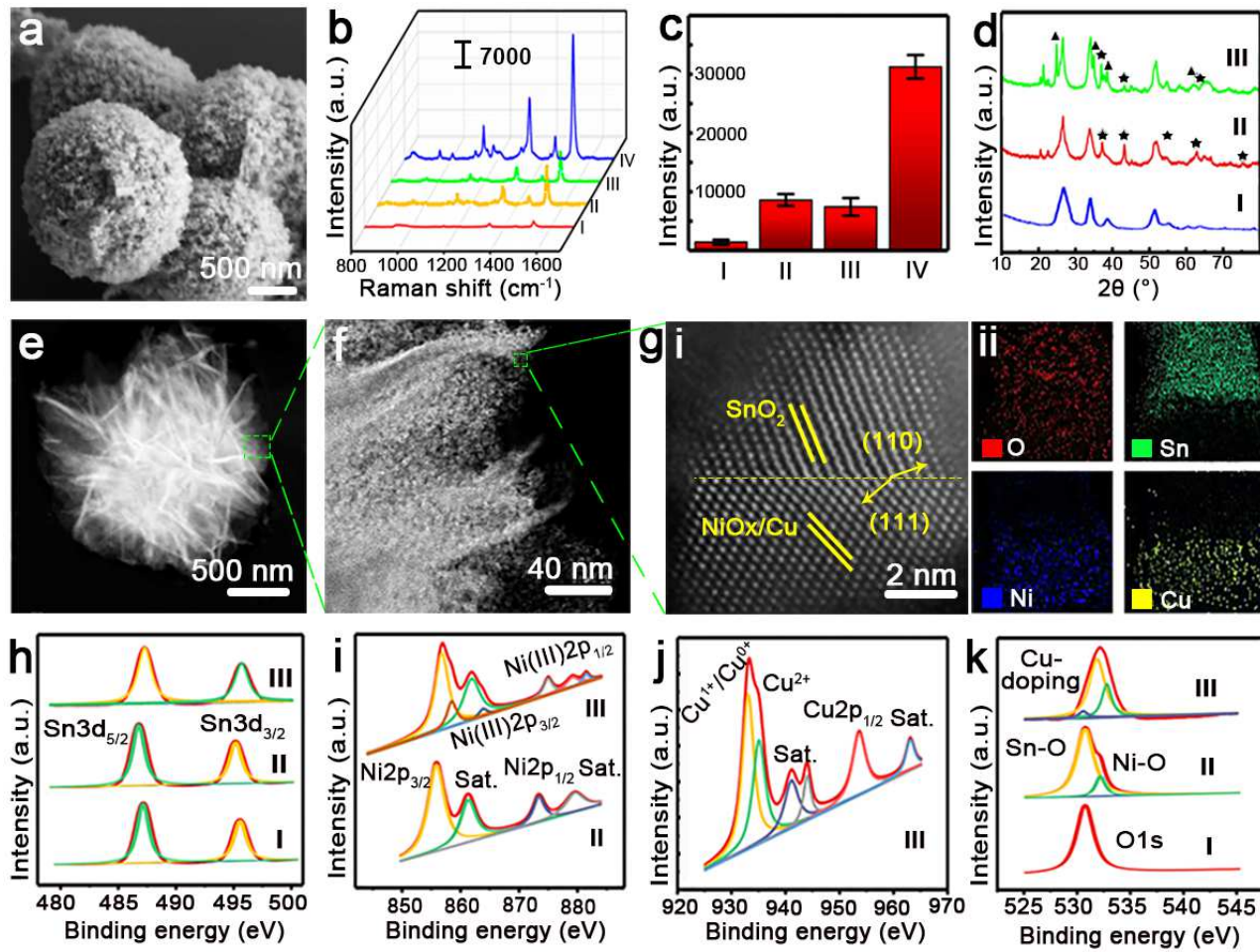


Fig. 2 Characterization and SERS Performance of SnO₂-NiOx/Cu. **a**, SEM images of SnO₂-NiOx/Cu. **b**, Raman spectra and **c**, Corresponding Raman intensities (1530 cm⁻¹) of CuPc on (I) Si, (II) SnO₂, (III) SnO₂-NiO, and (IV) SnO₂-NiO/Cu substrates under 785 nm laser excitation. Each data point represents the average value from three replicating SERS spectra (S.D., n = 6). **d**, XRD patterns of (I) SnO₂, (II) SnO₂-NiO and (III) SnO₂-NiOx/Cu. The NiO and Cu₂O/CuO peaks are marked with asterisks and triangles, respectively. **e**, Large-scale and **f**, magnified view of Aberration-corrected STEM-HAADF images of SnO₂-NiOx/Cu. **g-i**, Atomic resolution HAADF image and **g-ii**, corresponding EDS mapping images of SnO₂-NiOx/Cu. Core-level XPS spectra of **h**, Sn 3d, **i**, Ni 2p, **j**, Cu, and **k**, O 1s of (I) SnO₂, (II) SnO₂-NiO, and (III) SnO₂-NiOx/Cu, respectively.

resolved on the ligaments in HAADF image (Fig. 2g (i)). Both SnO₂ and NiOx/Cu were well crystallized without dislocations or other visible extended defects. The boundary between SnO₂ and NiOx/Cu marked on HAADF image also revealed the heteroepitaxy observed at the nanometer scale. This polycrystalline feature of SnO₂-NiOx/Cu was then confirmed by selected-area electron diffraction (SAED) (Supplementary Fig. 5b) and X-ray diffraction (XRD) pattern (Fig. 2d). The corresponding ACSTEM energy dispersive spectroscopy (EDS) mapping illustrated that Sn atoms were uniformly distributed across one side of heterojunction boundary while Ni and Cu atoms were distributed over the other side (Fig. 2g (ii)), indicating that Cu was only doped into NiO instead of SnO₂.

Next, X-ray photoelectron spectroscopy (XPS) was performed to elucidate the chemical bonding in SnO₂-NiOx/Cu nanosponge. As shown in Fig. 2h, two peaks observed at 486.9 (Sn 3d_{5/2}) and 495.3 eV (3d_{3/2}), and their spin-orbit splitting (8.4 eV) indicated the presence of Sn⁴⁺ in SnO₂-NiOx/Cu²⁰. A slight blue-shift of Sn 3d binding energy in SnO₂-NiOx/Cu compared with SnO₂, indicated that there was electronic interaction between SnO₂ and NiO. The core-level XPS of Ni 2p in SnO₂-NiOx/Cu was given in Fig. 2i,

where two emission peaks were centered at 853.2 eV (Ni (II) 2p_{3/2}) and 872.4 eV (Ni(II) 2p_{1/2}), respectively²¹. Besides, in comparison with SnO-NiO, another two new peaks at 857.1 and 874.8 eV were observed, which were assigned to Ni(III) 2p_{3/2} and Ni(III) 2p_{1/2}²¹. The results suggested that Cu doping in SnO₂-NiOx/Cu altered the Ni surrounding chemical environments. XPS data of Cu showed the binding energy of Cu 2p_{3/2} for SnO₂-NiOx/Cu at 932.5 and 933.3 eV, which were consistent with the divalent states of Cu⁺ and Cu²⁺ (Fig. 2)²². From O 1s XPS spectrum of SnO₂-NiOx/Cu, three peaks were clearly observed, in which O1s peak at 532.2 eV was ascribed to the lattice oxygen (O²⁻), while the high binding energy (533.3 eV) was assigned to the adsorbed oxygen ions (O²⁻ and O⁻) on the surface²³, which were consistent with those of SnO₂-NiO. In addition, another peak at the lower energy (531.0 eV) was attributed to the vacant oxygen (O_v)²⁴, indicating that Cu doping induced a large number of O_v in SnO₂-NiOx/Cu. These obvious changes indicated the existence of interaction between n-type SnO₂ and p-type NiOx/Cu, resulting in an efficient CT process between Raman reporter and SnO₂-NiOx/Cu SERS substrate.

Mechanism of Raman enhancement in SnO₂-NiOx/Cu

The CT process between SnO₂-NiOx/Cu and CuPc was then investigated through TDR spectroscopic measurements. Excited by 785 nm laser, the absorption bands centered at 530 nm were observed for CuPc-SnO₂, CuPc-SnO₂-NiO and CuPc-SnO₂-NiOx/Cu systems, which were assigned to trapped electrons (Supplementary Fig. 7). Time profiles of the transient absorption were fitted by two-exponential functions (Fig. 3a). The decay lifetime of electrons in CuPc-SnO₂-NiOx/Cu (1236.39 ps) was much longer than that in CuPc-SnO₂ (433.82 ps) and CuPc-SnO₂-NiO (325.37 ps), suggesting that p-n junction doped by Cu at SnO₂-NiOx/Cu interface acted as an electron trap site and led to efficient CT. To further explain TDR results, we investigated the electronic structure and the coupling of CuPc and SnO₂-NiOx/Cu as well as the consequent CT using DFT calculations. As shown in Fig. 3b, the amount of electron transfer from CuPc to SnO₂-NiOx/Cu (1.32 e⁻) was much more than that on SnO₂-NiO (0.68e⁻) or SnO₂ (0.87 e⁻). Both TDR results and DFT calculations provided strong evidence for effective CT between SnO₂-NiOx/Cu and CuPc, resulting in significant enhancement of Raman activity for CuPc on SnO₂-NiOx/Cu substrate.

As well known, the CM-based SERS effect strongly depends on the matching degree of the energy level between molecules and substrates⁷. To further elucidate the CT process, we determined CB and VB of SnO₂, NiO and NiOx/Cu, and highest occupied molecular orbital (HOMO) and lowest unoccupied molecular orbital (LUMO) levels of CuPc using DFT calculations. As shown in Fig. 3c, the calculation result was in a good agreement with that of the standard Tauc plot method (Supplementary Fig. 8). Without Cu doping, the energy barriers between VB of NiO or SnO₂ substrates and HOMO of CuPc were 2.2 and 2.1 eV, which were much greater than the energy of 785-nm laser (1.58 eV). Thus, the photon energy of 785 nm laser failed to excite the electrons at VB of the substrate into HOMO of CuPc and hard to separate electron-hole pairs effectively, thus leading to very weak Raman signals. However, the introduction of O_v created by Cu doping shifted the Fermi level of NiO toward CB and narrowed the band gap¹³. Under this situation, electrons at VB of NiOx/Cu substrate were excited and transferred into HOMO of CuPc successfully. Meanwhile, the energy difference between VB of NiOx/Cu and SnO₂ in CuPc-SnO₂-NiOx/Cu nanosystem was 1.5 eV, which was close to 1.58 eV. In this case, CT resonance occurred, leading to an obvious Raman enhancement on SnO₂-NiOx/Cu (Fig. 3d).

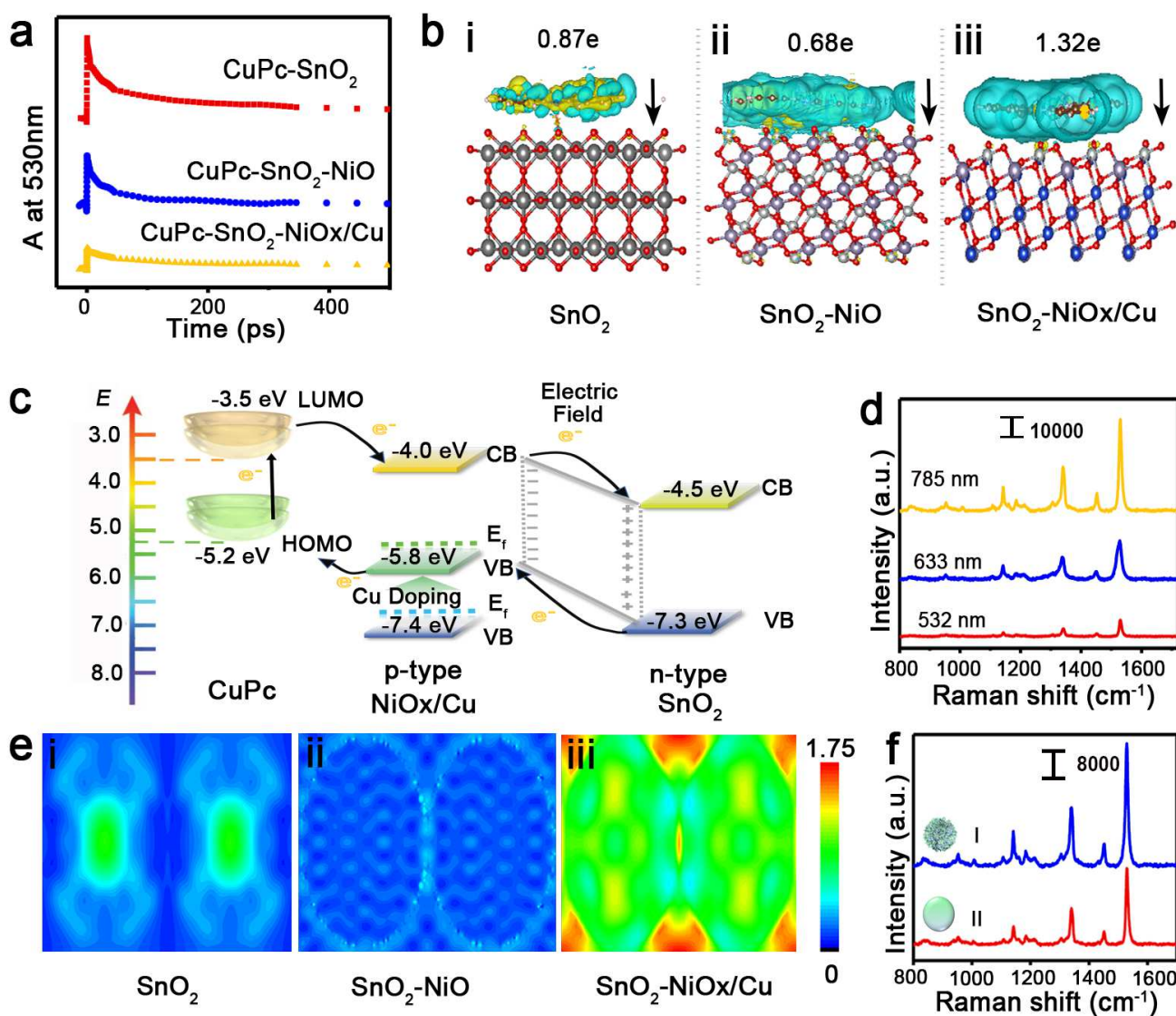


Fig. 3 Mechanism of Raman enhancement on SnO₂-NiOx/Cu. **a**, Time profiles of normalized transient absorption at 530 nm. **b**, Electron density difference $\delta\rho(r)$ of CuPc on (i) SnO₂, (ii) SnO₂-NiO, and (iii) SnO₂-NiOx/Cu: isosurfaces taken at 0.004 e Angstrom⁻³. Yellow means gaining electron, blues mean losing electron. **c**, Energy level diagram of CuPc molecule adsorbed on SnO₂-NiOx/Cu SERS substrate. **d**, Raman spectra of CuPc on SnO₂-NiOx/Cu under 532 nm, 633 nm, and 785 nm laser excitation (laser power: 5 mW, exposure time: 0.5 s, 50X lens). **e**, Electric near-field distribution around (i) SnO₂, (ii) SnO₂-NiO, and (iii) SnO₂-NiOx/Cu at a 785 nm excitation. **f**, Raman spectra of CuPc on (I) SnO₂-NiOx/Cu and (II) SnO₂-NiOx/Cu with compact surface under a 785 nm laser (5mW) with an exposure time of 0.5 s.

Significantly, the selective Cu doping on NiO narrowed the band gap through Fermi-level alignment, resulting in the conversion from type-I SnO₂-NiO heterojunction into type-II SnO₂-NiOx/Cu heterojunction. As for type I SnO₂-NiO semiconductor, the band of SnO₂ was embedded within that of NiO so that photogenerated electrons and holes were both concentrated in SnO₂. After Cu doping, the Fermi-level of NiOx/Cu lay closer to CB (Fig. 3c). Electrons in n-type SnO₂ filled some of the holes in p-type NiOx/Cu because these holes were available at lower-energy states. This left positively charged holes in n-type SnO₂ and extra negatively charged electrons in p-type NiOx/Cu²⁵. Thus, an inner electric field was formed at the equilibrium (Fig. 3c). Driven by the internal field, holes at VB of SnO₂ were excited into VB of NiOx/Cu, and electrons were accelerated from CB of NiOx/Cu into CB of SnO₂. In this case,

photogenerated electron-hole pairs were effectively separated by type II SnO₂-NiOx/Cu p-n junction between NiOx/Cu and SnO₂, realizing efficient spatial charge separation and prolongating the lifetime of charge carriers²⁶, and further enhancing the SERS activity. In order to confirm the effect of p-n junction on Raman enhancement for SnO₂-NiOx/Cu, SnO₂-In₂S₃ porous nanocomposite with non-p-n junction was synthesized, in which CB and VB levels of n-type In₂S₃ (-3.7 eV and -5.7 eV) were close to that of p-type NiOx/Cu. TDR results showed that electrons decay lifetime in CuPc-SnO₂-In₂S₃ (588.65 ps) was much shorter than that in CuPc-SnO₂-NiOx/Cu, indicating that p-n junction in SnO₂-NiOx/Cu acted as an electron trap site and led to more efficient CT (Supplementary Fig. 9a and b). Thus, compared with SnO₂-NiOx/Cu, obvious decline (30%) in SERS intensity of CuPc was observed on SnO₂-In₂S₃ porous nanocomposites (Supplementary Fig. 9c). Consequently, such synergetic promotion of CT resonance and type II p-n heterojunction formation in SnO₂-NiOx/Cu led to a high CT efficiency, further resulting in a remarkable SERS enhancement.

The above theoretical and experimental results revealed that the ultrahigh Raman enhancement on SnO₂-NiOx/Cu was mainly derived from CT mechanism. To clarify whether EM mechanism can be observed in SnO₂-NiOx/Cu substrate, finite difference time domain method (FDTD) was used to simulate and calculate the EM field distribution under 785-nm excitation for SnO₂, SnO₂-NiO and SnO₂-NiOx/Cu. As shown in Fig. 3e, SnO₂-NiOx/Cu obtained stronger electric near-field than SnO₂ or SnO₂-NiO. The reason was that Cu doping led to the generation of a high density of holes in VB of NiOx/Cu, sustaining an localized surface plasmon response (LSPR) in the near infrared (NIR) region. However, the EM effect on SERS enhancement was very limited, which was 8 orders of magnitude lower than the CM effect. (Supplementary Fig. 10).

Moreover, the Brunauer-Emmett-Teller surface area and pore size of as-prepared SnO₂-NiOx/Cu nanosponge were calculated to be as high as 26.16 m² g⁻¹ and 3.8 ± 0.3 nm (Supplementary Fig. 11), which was similar to that obtained from SEM image. Owing to CuPc enrichment by this porous structure, the SERS effect of as-prepared SnO₂-NiOx/Cu for CuPc was 1.8 times higher than that of SnO₂-NiOx/Cu with compact surface (Fig. 3f). Consequently, the remarkable EF of SnO₂-NiOx/Cu should be mainly ascribed to 3 factors: efficient CT process attributed to (i) type II p-n junction in SnO₂-NiOx/Cu for charge collection and separation, (ii) CT resonance under 785-nm laser excitation, and as well as (iii) the molecule enrichment by porous SnO₂-NiOx/Cu nanosponge.

VOCs detection of human EB based on the SERS nose

The SnO₂-NiOx/Cu nanosponge with high EF was then developed as a SERS nose (SnO₂-NiOx/Cu-CuPc) through immobilization of CuPc for sensitive and selective VOCs analysis. Herein, Raman intensity of CuPc at 1530 cm⁻¹ was employed as an inner-reference for improving the determination accuracy. The SnO₂-NiOx/Cu-CuPc SERS nose was versatile and employed to discern a series of toxic VOCs overexpressed in the EB of early stage lung cancer patients²⁷⁻²⁹, such as pyrene (PYR), 2-naphthalenethiol (2-NT) and 4-ethylbenzaldehyde (EBZA). Taking full advantage of fingerprint Raman peaks of these three molecules for quantitative analysis and the well matching degree of energy level between three target molecules and SnO₂-NiOx/Cu (Fig. 4a), the developed SERS nose showed excellent selectivity for VOCs sensing. The distinctive peak of PYR at 1236 cm⁻¹ indexed to CH in-plane bending vibrations

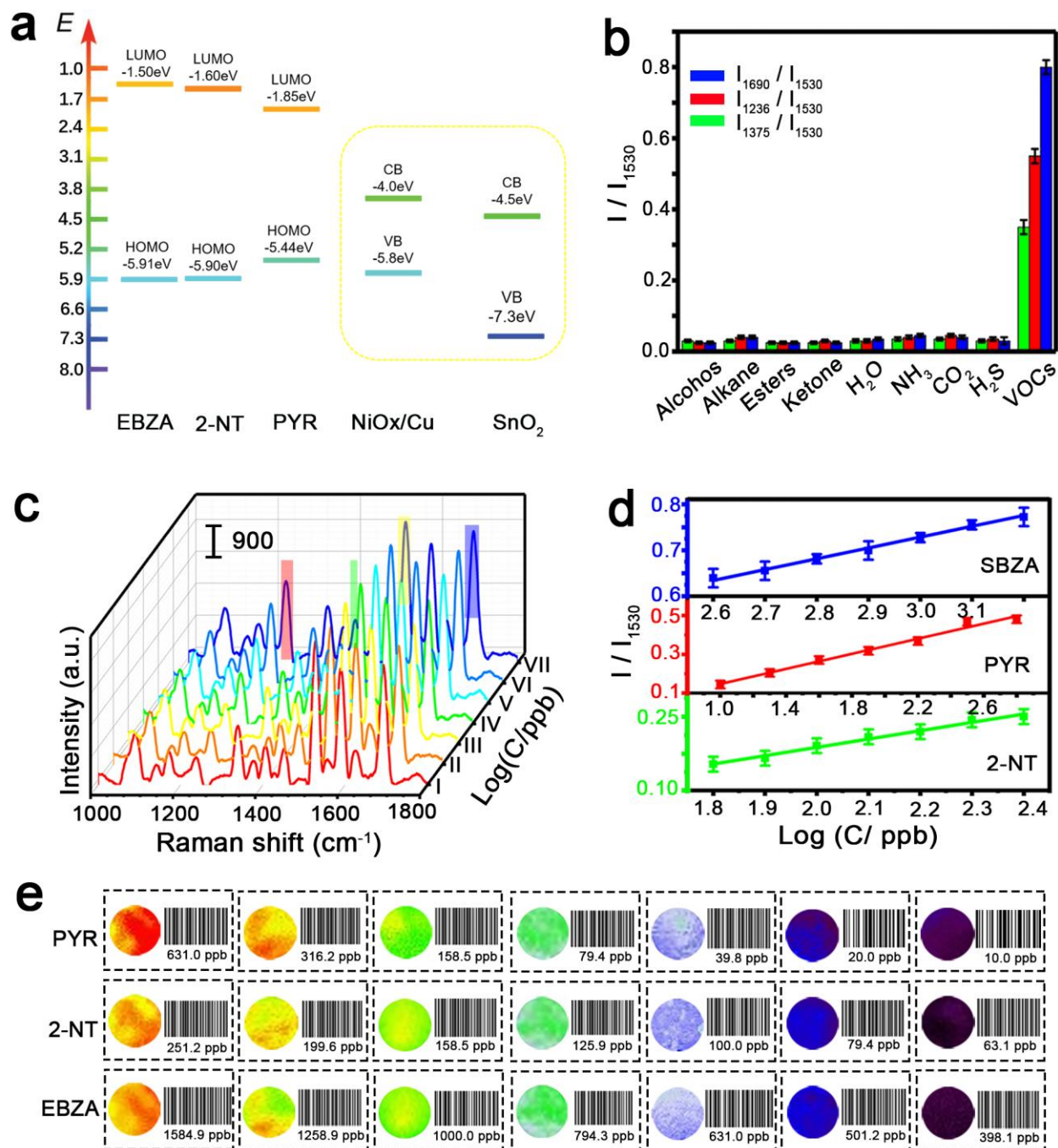


Fig. 4 SnO₂-NiOx/Cu-CuPc SERS nose for VOCs sensing. **a**, HOMO and LUMO of EBZA, 2-NT and PYR; CB and VB of SnO₂-NiOx/Cu. **b**, Selectivity tests of various relevant analytes against PYR, 2-NT and EBZA. **c**, Raman spectra of SnO₂-NiOx/Cu-CuPc obtained with PYR (I-VII: 10, 10^{1.3}, 10^{1.6}, 10^{1.9}, 10^{2.2}, 10^{2.5} and 10^{2.8} ppb), 2-NT (I-VII: 10^{1.8}, 10^{1.9}, 10^{2.0}, 10^{2.1}, 10^{2.2}, 10^{2.3} and 10^{2.4} ppb) and EBZA (I-VII: 10^{2.6}, 10^{2.7}, 10^{2.8}, 10^{2.9}, 10^{3.0}, 10^{3.1} and 10^{3.2} ppb) at various concentrations. **d**, Calibration curves of PYR, 2-NT and EBZA on a semilog scale. **e**, SERS mapping images obtained at peak intensity of 1236 cm⁻¹ for PYR, 1375 cm⁻¹ for 2-NT and 1690 cm⁻¹ for EBZA with different concentrations. The corresponding barcode was acquired based on the concentrations of VOCs and the R, G, and B values obtained from Raman mapping.

(δ_{C-H})³⁰. For 2-NT, the peak at 1375 cm⁻¹ corresponded to C=C stretching ($\nu_{C=C}$)³¹, while EBZA was identified by the peak at 1690 cm⁻¹ ($\nu_{C=O}$)³² (Supplementary Fig. 12). However, no obvious responses were obtained for other potential interferences in a mixed mimetic exhalation, including alkane, alcohols, esters, ketone, H₂O, NH₃, CO₂ and H₂S (Fig. 4b).

Since no cross reactions were observed for determination of PYR, 2-NT and EBZA (Supplementary Fig. 13), these three VOCs were then simultaneously detected using this SERS nose. The SERS intensity ratio (I_{1236}/I_{1530} , I_{1375}/I_{1530} and I_{1690}/I_{1530}) showed a good linearity with logarithmic VOC concentration over the range from 10 ppb to 1000 ppm, due to Temkin adsorption of VOCs on SERS substrates³³ (Supplementary Fig. 12). The limits of detection (LODs) were estimated to be 7.6 ± 0.7 , 5.3 ± 0.6 , and 4.1 ± 0.5 ppb for PYR, 2-NT and EBZA, respectively, which were 10 times lower than those obtained by GC-MS¹² and fluorescence spectroscopy¹³, 100 times lower than those obtained by electrochemical methods¹⁴ (Supplementary Table 2). Considering that the VOC concentration in human EB samples was below 2 ppm, we measured I/I_{1530} of each VOC more accurately in narrow ranges (PYR: $10\text{-}10^{2.8}$ ppb, 2-NT: $10^{1.8}\text{-}10^{2.4}$ ppb and EBZA: $10^{2.6}\text{-}10^{3.2}$ ppb) (Fig. 4c and 4d). Subsequently, two-dimensional Raman mapping images were obtained based on the peak intensities of 1236, 1375, and 1690 cm^{-1} corresponding to PYR, 2-NT and EBZA by scanning Raman signals with a computer-controlled x-y translational stage (Fig. 4e). The color of Raman images remarkably changed from purple to red with

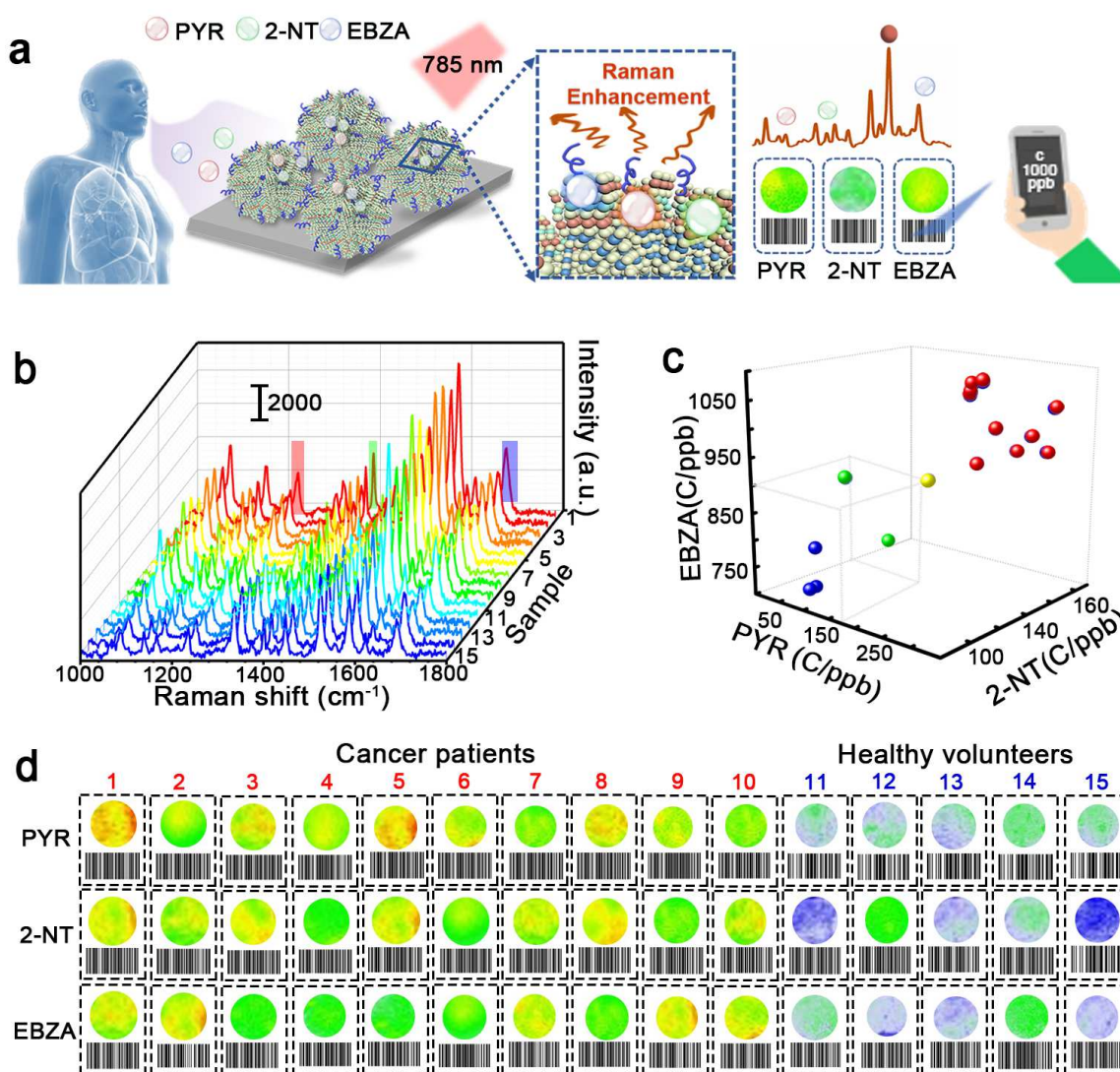


Fig.5 SnO₂-NiOx/Cu-CuPc SERS nose for VOCs sensing in human EB samples. **a**, Diagram of SnO₂-NiOx/Cu-CuPc SERS nose for VOCs sensing. **b**, SERS spectra, **c**, bubble chart of the diagnosis results and **d**, Raman mapping and corresponding barcode of EB samples for lung cancer patients (1-10) and healthy groups (11-15).

increasing concentration of these VOCs. Then, the VOC concentration information was automatically transformed into an optical, machine readable barcode by integrating R, G, B values of Raman images and reading concentrations based on linear curves (Supplementary Fig. 14). Hence, the composition and concentration information on VOCs were integrated to yield barcodes that can be read rapidly and conveniently by a barcode scanner. Meanwhile, the SERS nose showed a good stability within 3 months (< 4.21 %) and a satisfying reproducibility with RSDs below 3.18% (n=5) (Supplementary Fig. 15). These results demonstrated that the present SERS nose provided good sensitivity, specificity and stability for multiple VOC detection at ~ppb levels.

Furthermore, we took advantage of the developed SERS nose to demonstrate the simultaneous detection of PYR, 2-NT and EBZA in the EB of early stage lung cancer patients (Fig. 5a). Fig. 5b and 5d show SERS spectra and corresponding barcodes of EB samples for 10 lung cancer patients and 5 healthy people. A regression analysis between the proposed SERS nose and GC-MS was conducted to demonstrate its utility (Supplementary Fig. 16). Compared with single-VOC tests, the simultaneous detection of three VOCs improved the reliability and avoid false positive diagnoses (Fig. 5c). With the aid of multiple VOC detection based on SnO₂-NiOx/Cu-CuPc SERS nose, the diagnosis and screening of lung cancer can be conducted in a single fast, easy and cost-effective assay, thus affording an ideal test method for point of care detection.

Discussion

In this work, a novel sponge-like SnO₂-NiOx/Cu-CuPc SERS nose was first developed for ultrasensitive and selective recognition of multiple VOCs down to ppb level. First of all, the sponge like SnO₂-NiOx/Cu type II p-n semiconductor heterostructure, which was verified by ACSTEM and Mott-Schottky plots, was synthesized using a hydrothermal method combined with a subsequent calcination. The EF value of SnO₂-NiOx/Cu for CuPc was achieved up to 1.66×10^{10} , the highest EF value for CM-based SERS substrates reported by far. Both experimental results and theoretical calculations revealed that the SERS enhancement was mainly stemmed from efficient charge separation by SnO₂-NiOx/Cu p-n heterojunction and charge transfer resonance caused by Cu doping, which enhanced charge transfer efficiency between SnO₂-NiOx/Cu substrate and probe molecules. Besides, enrichment of probe molecules from porous sponge structure further magnified SERS signals. Then, by immobilizing of CuPc molecule as an inner-reference element, the SnO₂-NiOx/Cu substrate was developed as a SERS nose (SnO₂-NiOx/Cu-CuPc) for VOCs analysis with high sensitivity, selectivity, and accuracy. The developed SERS nose was able to 'sniff out' and simultaneously quantify multiple toxic VOCs in the EB of early stage lung cancer patients at ppb level, which was 10 times lower than those obtained by GC-MS and fluorescence spectroscopy, 100 times lower than that obtained by electrochemical method. Unique barcodes denoting the VOCs concentrations were obtained by integrating R, G, and B values of the Raman intensity images, where these barcodes can be easily read by electronic devices, such as smartphones and handheld scanners. This work has provided a methodology for designing and synthesizing p-n heterostructures to enhance Raman signals and has demonstrated the practical potential of a desktop SERS device for biomarker screening. This established method can also be extended to monitor the levels of other VOCs, which are related to diabetes, advanced liver disease, kidney failure, and lung abscess.

References

1. Goldberg-Oppenheimer, P., Mahajan, S. & Steiner, U. Hierarchical electrohydrodynamic structures for surface-enhanced Raman scattering. *Adv. Mater.* **24**, OP175-OP180 (2012).
2. Yu, S. et al. Plasmon near-field coupling of bimetallic nanostars and a hierarchical bimetallic SERS “hot field”: toward ultrasensitive simultaneous detection of multiple cardiorenal syndrome biomarkers. *Anal. Chem.* **91**, 864-872 (2019).
3. Anker, J. N. et al. Biosensing with plasmonic nanosensors. *Nat. Mater.* **7**, 442-453 (2008).
4. Qiu, B., Xing, M., Yi, Q. & Zhang, J. Chiral carbonaceous nanotubes modified with titania nanocrystals: Plasmon-free and recyclable SERS sensitivity. *Angew. Chem. Int. Ed.* **54**, 10643-10647 (2015).
5. Lin, J. et al. Ultrasensitive SERS detection by defect engineering on single Cu₂O superstructure particle. *Adv. Mater.* **29**, 1604797 (2017).
6. Feng, E., Zheng, T., He, X., Chen, J. & Tian, Y. A novel ternary heterostructure with dramatic SERS activity for evaluation of PD-L1 expression at the single-cell level. *Sci. Adv.* **4**, eaau3494 (2018).
7. Ganesh, S., Venkatakrishnan, K. & Tan, B. Quantum scale organic semiconductors for SERS detection of DNA methylation and gene expression. *Nat. Commun.* **11**, 1135 (2020).
8. Yilmaz, M. et al. Nanostructured organic semiconductor films for molecular detection with surface-enhanced Raman spectroscopy. *Nat. Mater.* **16**, 918-924 (2017).
9. Lee, S. H., Nishi, H. & Tatsuma, T. Plasmonic behaviour and plasmon-induced charge separation of nanostructured MoO_{3-x} under near infrared irradiation. *Nanoscale* **10**, 2841-2847 (2018).
10. Yu, X., Marks, T. J. & Facchetti, A. Metal oxides for optoelectronic applications. *Nat. Mater.* **15**, 383-396 (2016).
11. Zhang, C. et al. Strain distributions and their influence on electronic structures of WSe₂-MoS₂ laterally strained heterojunctions. *Nat. Nanotechnol.* **13**, 152-158 (2018).
12. Li, Q. et al. Two-dimensional morphology enhances light-driven H₂ generation efficiency in CdS nanoplatelet-Pt heterostructures. *J. Am. Chem. Soc.* **140**, 11726-11734 (2018).
13. Ji, S., Gu, S., Wang, X. & Wu, N. Comparison of olfactometrically detected compounds and aroma properties of four different edible parts of Chinese mitten crab. *Fish Sci.* **81**, 1157-1167 (2015).
14. Mohr, A. et al. A new pyrene-based fluorescent probe for the determination of critical micelle concentrations. *J. Phys. Chem. B* **111**, 12985-12992 (2007).
15. Penezić, A., Gašparović, B., Stipaničev, D. & Nelson, A. In situ electrochemical method for detecting freely dissolved polycyclic aromatic hydrocarbons in water. *Environ. Chem.* **11**, 173-180 (2014).
16. Jiang, N. et al. Observation of multiple vibrational modes in ultrahigh vacuum tip-enhanced Raman spectroscopy combined with molecular-resolution scanning tunneling microscopy. *Nano Lett.* **12**, 5061-5067 (2012).
17. Meng, F., Li, J., Cushing, S. K., Zhi, M. & Wu, N. Solar hydrogen generation by nanoscale p-n junction of p-type molybdenum disulfide/n-type nitrogen-doped reduced graphene oxide. *J. Am. Chem. Soc.* **135**, 10286-10289 (2013).
18. Zhu, Z. et al. Enhanced efficiency and stability of inverted perovskite solar cells using highly crystalline SnO₂ nanocrystals as the robust electron-transporting layer. *Adv. Mater.* **28**, 6478-6484 (2016).
19. Hoon, P. K. et al. Efficient CH₃NH₃PbI₃ perovskite solar cells employing nanostructured p-type NiO electrode formed by a pulsed laser deposition. *Adv. Mater.* **27**, 4013-4019 (2015).

20. Xin, Y., Kan, X., Gan, L. & Zhang, Z. Heterogeneous bimetallic phosphide/sulfide nanocomposite for efficient solar-energy driven overall water splitting. *ACS Nano* **11**, 10303-10312 (2017).
21. Simon, T. et al. Redox shuttle mechanism enhances photocatalytic H₂ generation on Ni-decorated CdS nanorods. *Nat. Mater.* **13**, 1013-1018 (2014).
22. Li, Y. et al. Enhancing oxidation resistance of Cu (I) by tailoring microenvironment in zeolites for efficient adsorptive desulfurization. *Nat. Commun.* **11**, 3206 (2020).
23. Zhang, Y. et al. Direct observation of oxygen vacancy self-healing on TiO₂ photocatalysts for solar water splitting. *Angew. Chem. Int. Ed.* **58**, 14229-14233 (2019),.
24. Wang, H. et al. Oxygen-vacancy-mediated exciton dissociation in BiOBr for boosting charge-carrier-involved molecular oxygen activation. *J. Am. Chem. Soc.* **140**, 1760-1766 (2018).
25. Wu, G. et al. Programmable transition metal dichalcogenide homojunctions controlled by nonvolatile ferroelectric domains. *Nat. Electron.* **3**, 43-50 (2020).
26. Wang, H. et al. Giant electron-hole interactions in confined layered structures for molecular oxygen activation. *J. Am. Chem. Soc.* **139**, 4737-4742 (2017).
27. Rodriguez-Aguilar, M. et al. Ultrafast gas chromatography coupled to electronic nose to identify volatile biomarkers in exhaled breath from chronic obstructive pulmonary disease patients: A pilot study. *Biomed. Chromatogr.* **33**, e4684 (2019).
28. Peled, N. et al. Non-invasive breath analysis of pulmonary nodules. *J Thorac Oncol.* **7**, 1528-1533 (2012).
29. Qiao, X. et al. Detection of exhaled volatile organic compounds improved by hollow nanocages of layered double hydroxide on Ag nanowires. *Angew. Chem. Int. Ed.* **58**, 1-6 (2019).
30. Yang, M. et al. SERS-active gold lace nanoshells with built-in hotspots. *Nano Lett.* **10**, 4013-4019 (2010).
31. Koh, C. S. L., Lee, H. K., Han, X., Sim, H. Y. F. & Ling, X. Y. Plasmonic nose: integrating the MOF-enabled molecular preconcentration effect with a plasmonic array for recognition of molecular-level volatile organic compounds. *Chem. Commun.* **54**, 2546-2549 (2018).
32. Conoci, S., Valli, L., Rella, R., Compagnini, G. & Cataliotti, R.S. A SERS study of self-assembled (4-methylmercapto) benzaldehyde thin films; *Mater. Sci. Eng., C* **22**, 183-186 (2002).
33. Belhaj, A. F. et al. Experimental investigation, binary modelling and artificial neural network prediction of surfactant adsorption for enhanced oil recovery application. *Chem. Eng. J.* **406**, 127081 (2021).

Methods

Methods are included in the Supplementary Information.

Data availability

The data that support the plots within this paper and other findings of this study are available from the corresponding author on reasonable request.

Author information

Affiliations

State Key Laboratory of Precision Spectroscopy, East China Normal University, Shanghai 200241, China

Yan Zhou, Jinquan Chen, Yang Tian

Shanghai Key Laboratory of Green Chemistry and Chemical Processes, Department of Chemistry, School of Chemistry and Molecular Engineering, East China Normal University, Shanghai, China

Qingyi Gu, Xiao He, Tingting Zheng, Yang Tian

Oncology department, Jiangsu Province Hospital, Nanjing, China

Tianzhu Qiu

Key laboratory of Polar Materials and Devices (MOE), Department of Optoelectronics, East China Normal University, Shanghai, China

Ruijuan Qi, Rong Huang

Shanghai Engineering Research Center of Molecular Therapeutics and New Drug Development, School of Chemistry and Molecular Engineering, East China Normal University, Shanghai, China

Xiao He

Author contributions

Yang Tian and Tingting Zheng conceived the research, designed the experiments and supervised the work. Yan Zhou fabricated materials and performed all the SERS experiments. Qingyi Gu and Xiao He conducted the DFT calculation. Jingquan Chen performed the TDR experiments. Tianzhu Qiu provided human EB samples and conducted corresponding experiments. Ruijuan Qi and Rong Huang completed the characterization of materials. Yan Zhou wrote the manuscript with Yang Tian and Tingting Zheng. All the authors were involved in the discussion and participated in manuscript input.

Corresponding author

Tingting Zheng - E-mail: tzheng@chem.ecnu.edu.cn.

Yang Tian – E-mail: ytian@chem.ecnu.edu.cn.

Competing interests

The authors declare no competing financial interest.

Acknowledgments

The authors greatly appreciate the financial support from NSFC (21827814 for Y. Tian, 21974049 for T. Zheng). This work also was supported by Innovation Program of Shanghai Municipal Education Commission (201701070005E00020) and Shanghai Rising-star Program (20QA1403300).

Figures

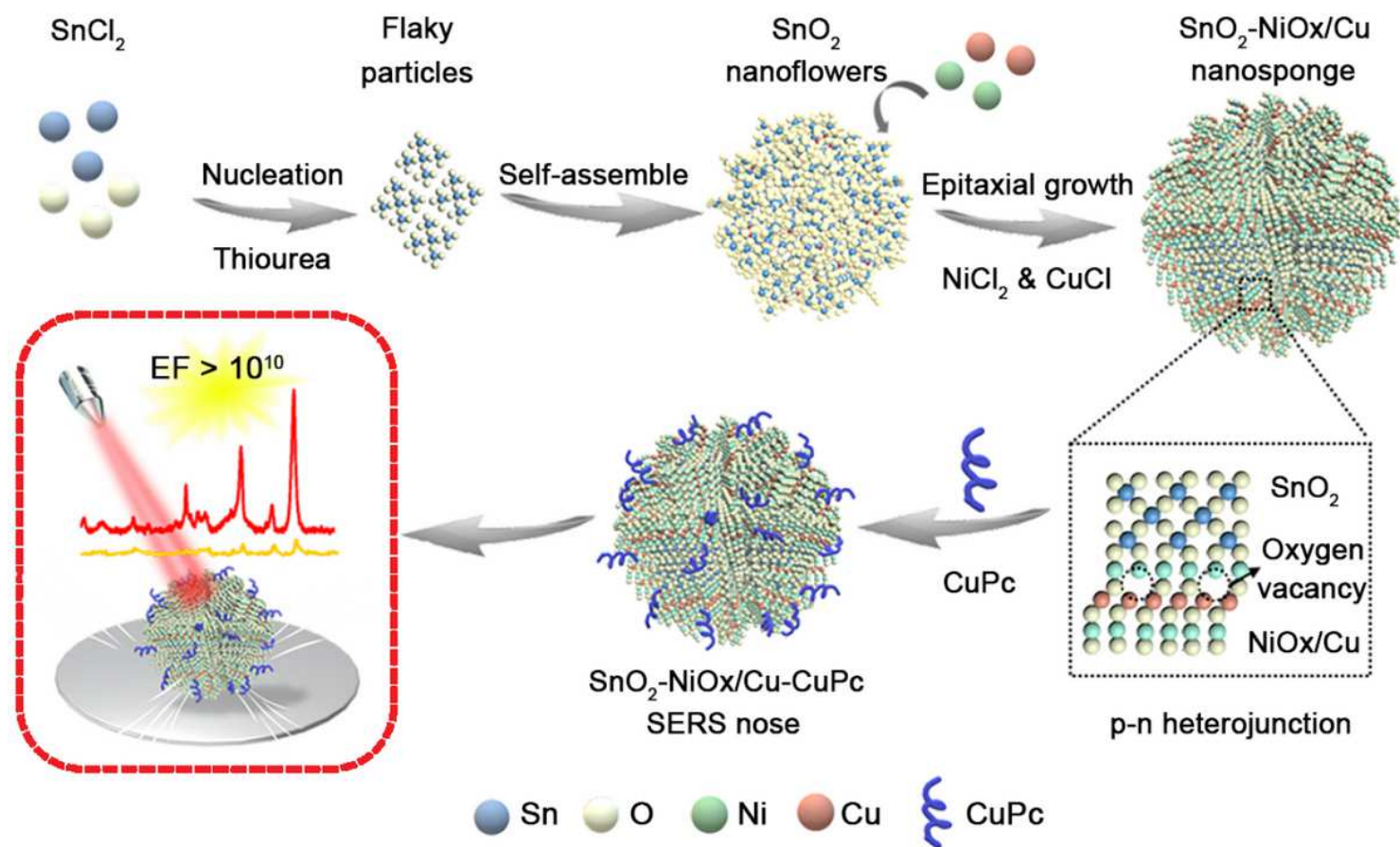


Figure 1

Design and synthesis of a sponge-like Cu-doping SnO₂-NiO p-n semiconductor heterostructure (SnO₂-NiOx/Cu) for Raman enhancement. SnO₂-NiOx/Cu nanosponge was obtained using a hydrothermal method combined with a subsequent calcination. It was designed and created as a CM-based SERS substrate with extremely high Raman enhancement ($EF=1.66 \times 10^{10}$) using CuPc as a prototype probe molecule under 785 nm laser excitation.

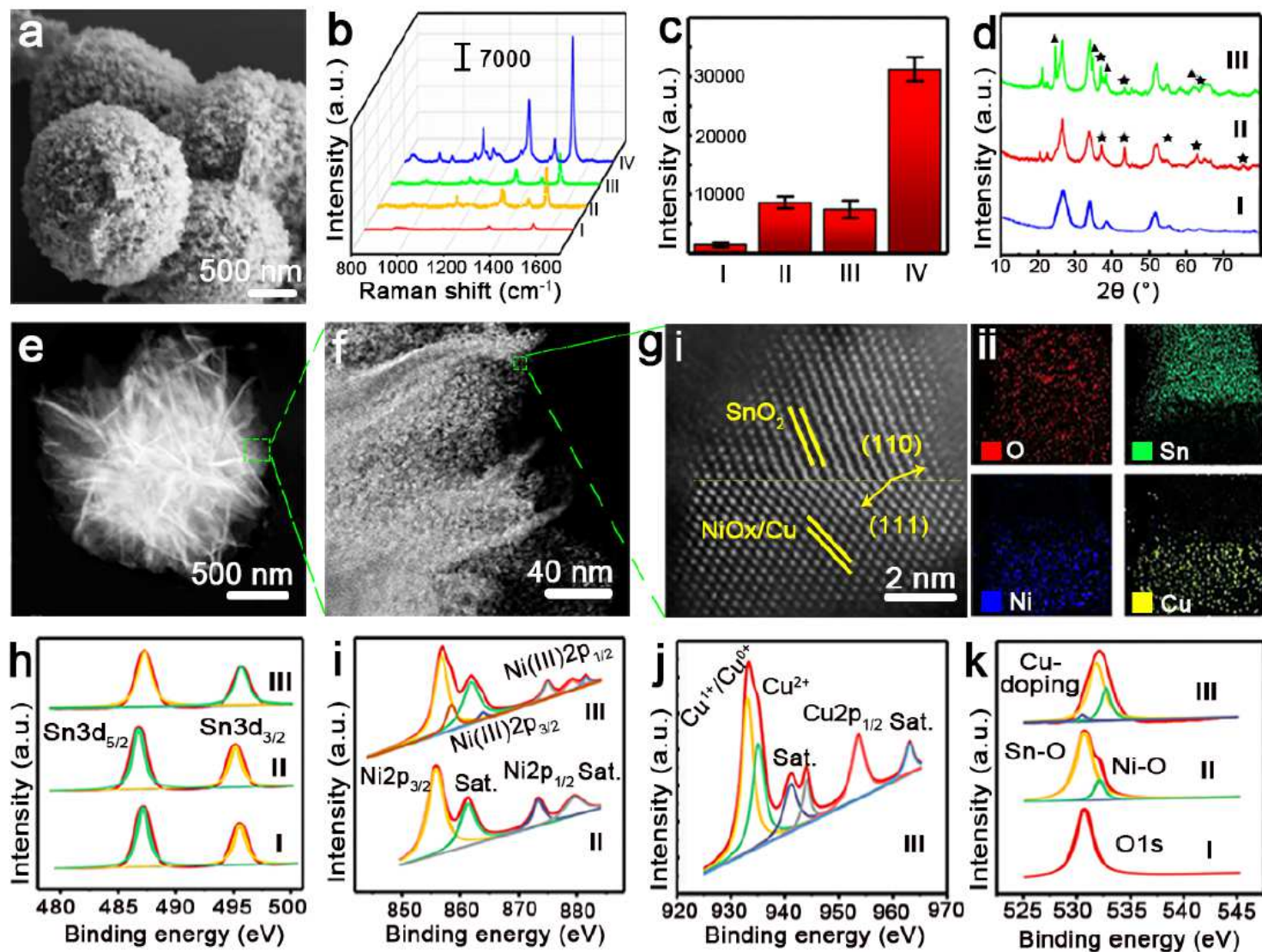


Figure 2

Characterization and SERS Performance of SnO₂-NiO_x/Cu. a, SEM images of SnO₂-NiO_x/Cu. b, Raman spectra and c, Corresponding Raman intensities (1530 cm⁻¹) of CuPc on (I) Si, (II) SnO₂, (III) SnO₂-NiO, and (IV) SnO₂-NiO_x/Cu substrates under 785 nm laser excitation. Each data point represents the average value from three replicating SERS spectra (S.D., n = 6). d, XRD patterns of (I) SnO₂, (II) SnO₂-NiO and (III) SnO₂-NiO_x/Cu. The NiO and Cu₂O/CuO peaks are marked with asterisks and triangles, respectively. e, Large-scale and f, magnified view of Aberration-corrected STEM-HAADF images of SnO₂-NiO_x/Cu. g-i, Atomic resolution HAADF image and g-ii, corresponding EDS mapping images of SnO₂-NiO_x/Cu. Core-level XPS spectra of h, Sn 3d, i, Ni 2p, j, Cu, and k, O 1s of (I) SnO₂, (II) SnO₂-NiO, and (III) SnO₂-NiO_x/Cu, respectively.

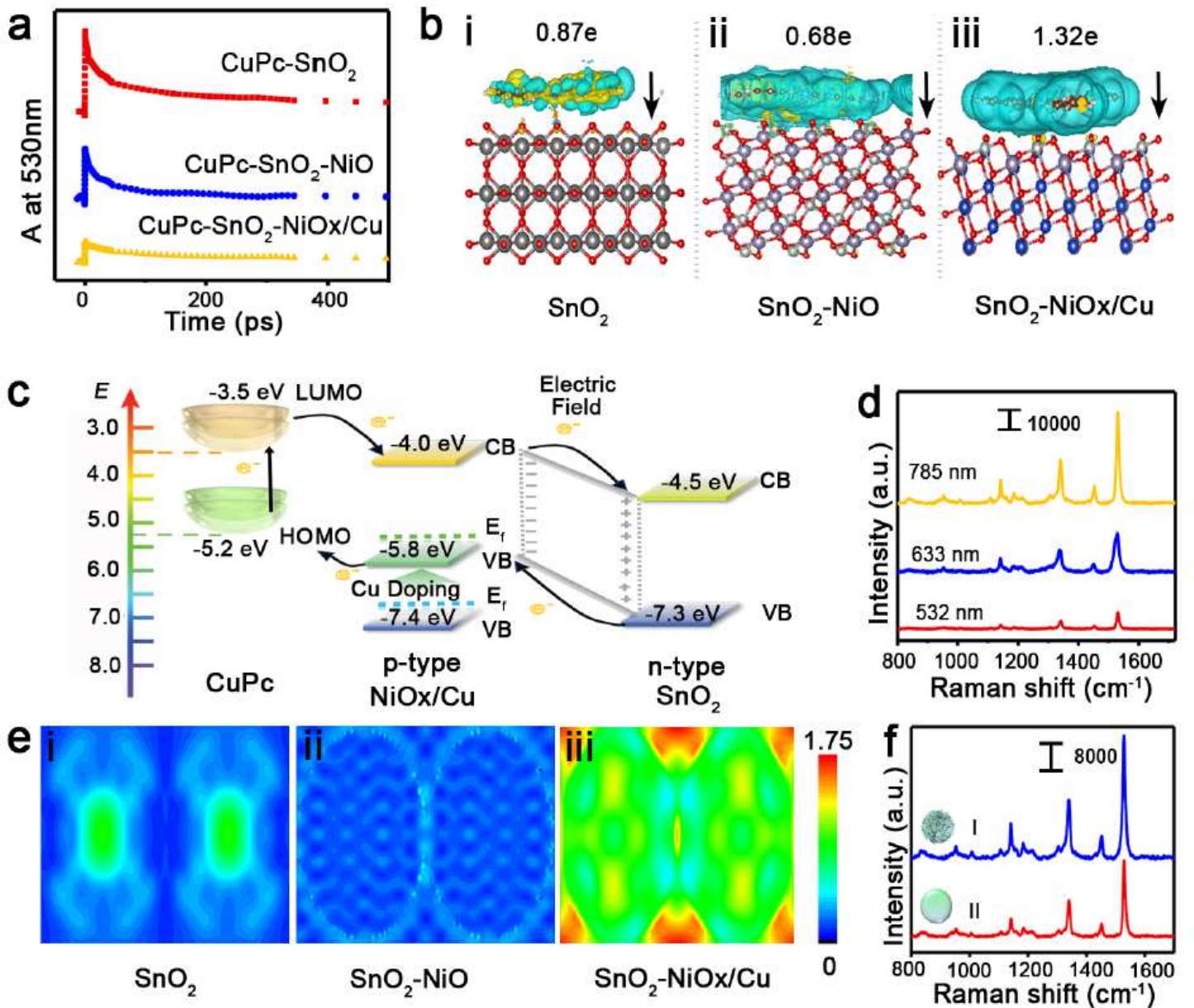


Figure 3

Mechanism of Raman enhancement on SnO₂-NiOx/Cu. a, Time profiles of normalized transient absorption at 530 nm. b, Electron density difference $\delta\rho(r)$ of CuPc on (i) SnO₂, (ii) SnO₂-NiO, and (iii) SnO₂-NiOx/Cu: isosurfaces taken at 0.004 e/Å³. Yellow means gaining electron, blues mean losing electron. c, Energy level diagram of CuPc molecule adsorbed on SnO₂-NiOx/Cu SERS substrate. d, Raman spectra of CuPc on SnO₂-NiOx/Cu under 532 nm, 633 nm, and 785 nm laser excitation (laser power: 5 mW, exposure time: 0.5 s, 50X lens). e, Electric near-field distribution around (i) SnO₂, (ii) SnO₂-NiO, and (iii) SnO₂-NiOx/Cu at a 785 nm excitation. f, Raman spectra of CuPc on (I) SnO₂-NiOx/Cu and (II) SnO₂-NiOx/Cu with compact surface under a 785 nm laser (5mW) with an exposure time of 0.5 s.

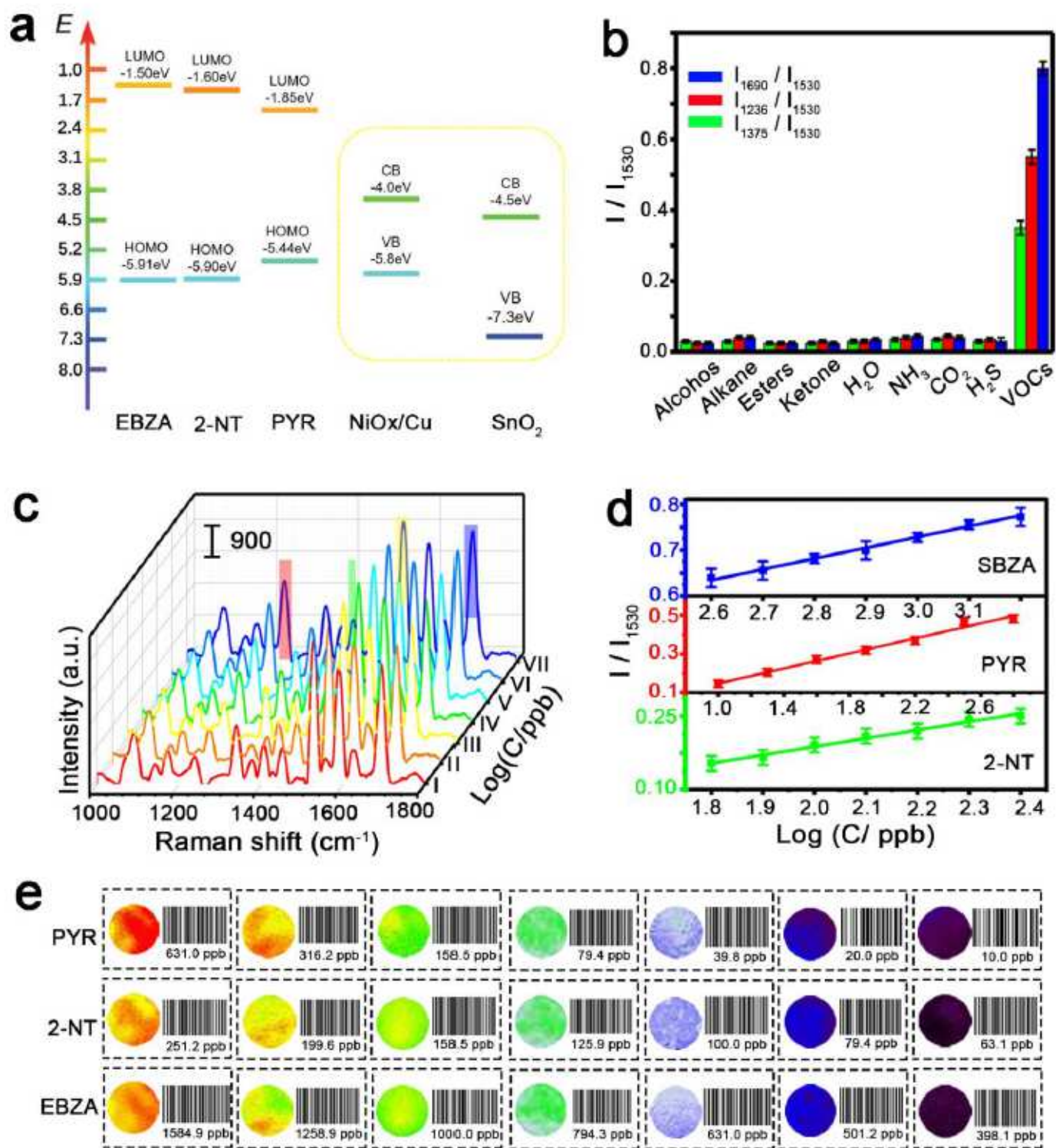


Figure 4

SnO₂-NiO_x/Cu-CuPc SERS nose for VOCs sensing. a, HOMO and LUMO of EBZA, 2-NT and PYR; CB and VB of SnO₂-NiO_x/Cu. b, Selectivity tests of various relevant analytes against PYR, 2-NT and EBZA. c, Raman spectra of SnO₂-NiO_x/Cu-CuPc obtained with PYR (I-VII: 10, 101.3, 101.6, 101.9, 102.2, 102.5 and 102.8 ppb), 2-NT (I-VII: 101.8, 101.9, 102.0, 102.1, 102.2, 102.3 and 102.4 ppb) and EBZA (I-VII: 102.6, 102.7, 102.8, 102.9, 103.0, 103.1 and 103.2 ppb) at various concentrations. d, Calibration curves of PYR,

2-NT and EBZA on a semilog scale. e, SERS mapping images obtained at peak intensity of 1236 cm^{-1} for PYR, 1375 cm^{-1} for 2-NT and 1690 cm^{-1} for EBZA with different concentrations. The corresponding barcode was acquired based on the concentrations of VOCs and the R, G, and B values obtained from Raman mapping.

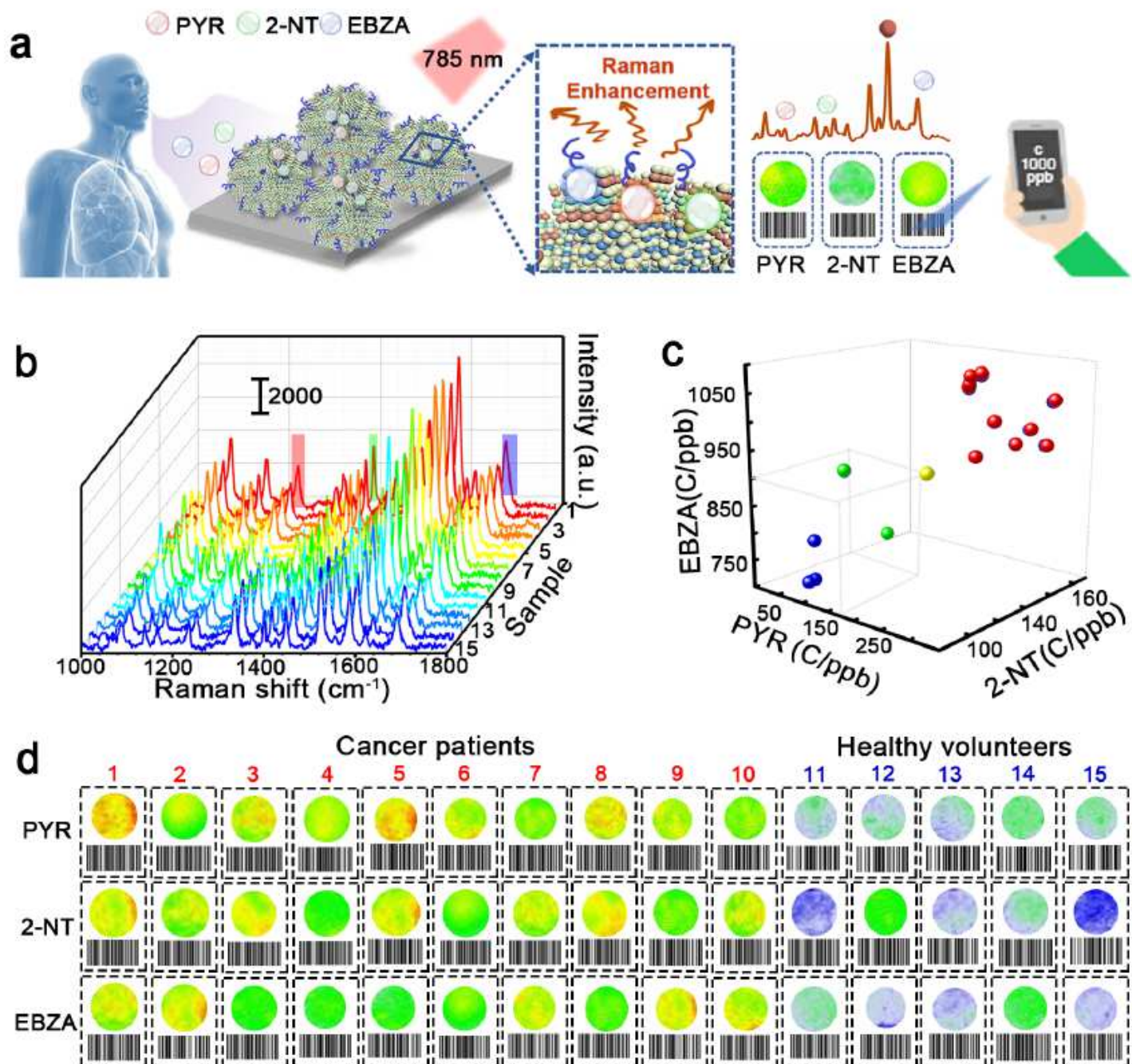


Figure 5

SnO₂-NiO_x/Cu-CuPc SERS nose for VOCs sensing in human EB samples. a, Diagram of SnO₂-NiO_x/Cu-CuPc SERS nose for VOCs sensing. b, SERS spectra, c, bubble chart of the diagnosis results and d, Raman mapping and corresponding barcode of EB samples for lung cancer patients (1-10) and healthy groups (11-15).

Supplementary Files

This is a list of supplementary files associated with this preprint. Click to download.

- [SupplementaryInformation.pdf](#)